Supplementary Information

Covalent netting restrains dissolution enabling stable high-loading and high-rate iron difluoride cathodes

Wenqiang Xu,‡[a,b] Yingjie Ma, ‡[b] Denghui Wang,[b,d] Siyuan Zhang,[b,d] Mathar Hamza,[b,d] Linjie Zhi,*[c] Lidong Li,*[a] and Xianglong Li*[b,d]

[a] State Key Laboratory for Advanced Metals and Materials, School of Materials Science and Engineering, University of Science and Technology Beijing, Beijing, 100083, China.

[b] CAS Key Laboratory of Nanosystem and Hierarchical Fabrication, CAS Center for Excellence in Nanoscience, National Center for Nanoscience and Technology, Beijing, 100190, China.

[c] State Key Laboratory of Heavy Oil Processing, Institute of New Energy, College of Chemical Engineering, China University of Petroleum (East China), Qingdao, 266580, China.

[d] University of Chinese Academy of Sciences, Beijing, 100049, China.

† These authors contributed equally: Wenqiang Xu, Yingjie Ma.

* Corresponding author, e-mail addresses: lidong@mater.ustb.edu.cn (L.L.), lixl@nanoctr.cn (X.L.) and zhilj@upc.edu.cn (L.Z.).

Note S1

As shown in Fig. 3c, the deconvoluted O 1s XPS spectrum of PBC@FeF_2@C exhibits four peaks located at approximate 530.1, 531.2, 532.3, and 533.7 eV, assignable to Fe-O-C, O=C, O-C, and HO-C bonds, respectively. By comparison, PBC@FeF_2 bears two peaks at 531.1 and 532.3 eV, corresponding to O=C and O-C bonds, respectively (Fig. 3d). In addition to validating Fe-O-C bonds in PBC@FeF_2@C, these peaks depict the presence of oxygen-containing functionalities within the carbon component of both PBC@FeF_2@C and PBC@FeF_2. This fact is mostly associated with the used carbon precursors (that is, BC and PDA in the former, and BC in the latter). In comparison with PBC@FeF_2, the additional occurrence of HO-C bonds can be attributed to the PDA carbon introduced. This is also the case for FeF_2@C (Fig. S6). The existence of these residual oxygen-containing functionalities in all the three cases is also verified by deconvoluting their C 1s spectra, in which three peaks consistently appear at approximate 284.7, 286.5, and 289.2 eV, characteristic of C-C/C=C C-O, and O=C-O bonds, respectively. Notably, a significant peak can be distinguished at 285.6 eV in the C 1s XPS spectrum of PBC@FeF_2@C (Fig. 3c), which can be assigned to C-N bonds, similar to that of FeF_2@C (Fig. S6). In sharp contrast, the corresponding peak is nearly negligible at the same binding energy in PBC@FeF_2 (Fig. 3d and Fig. S5), implying the absence of nitrogen. Furthermore, deconvolution of the N 1s XPS spectrum of PBC@FeF_2@C reveals three component peaks at 398.5, 400.2, and 401.4 eV, which can be ascribed to pyridinic N, pyrrolic N, and graphitic N species, respectively (Fig. S5a). This scenario is similarly found in FeF_2@C (Figure S6). Definitely, these findings manifest the nitrogen-doped nature of the PDA-derived carbon in PBC@FeF_2@C as well as FeF_2@C.

Supporting Figure

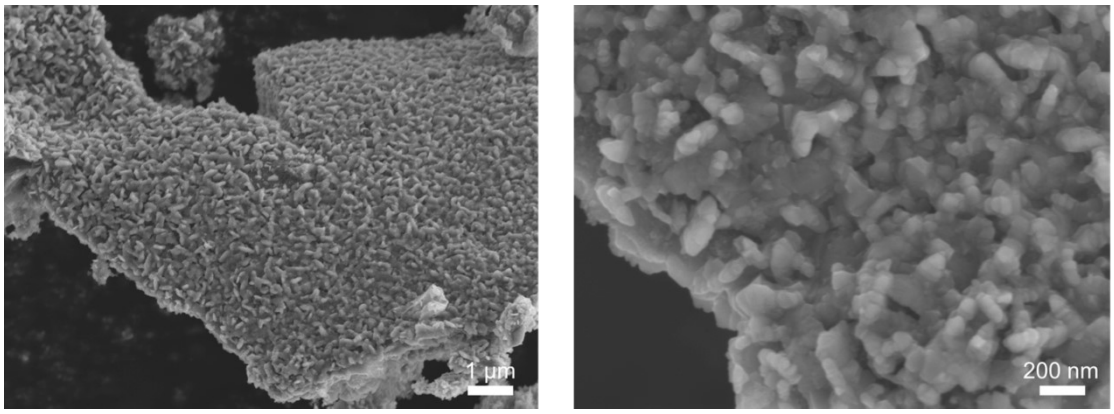

Fig. S1. SEM images of FeF_2@C.

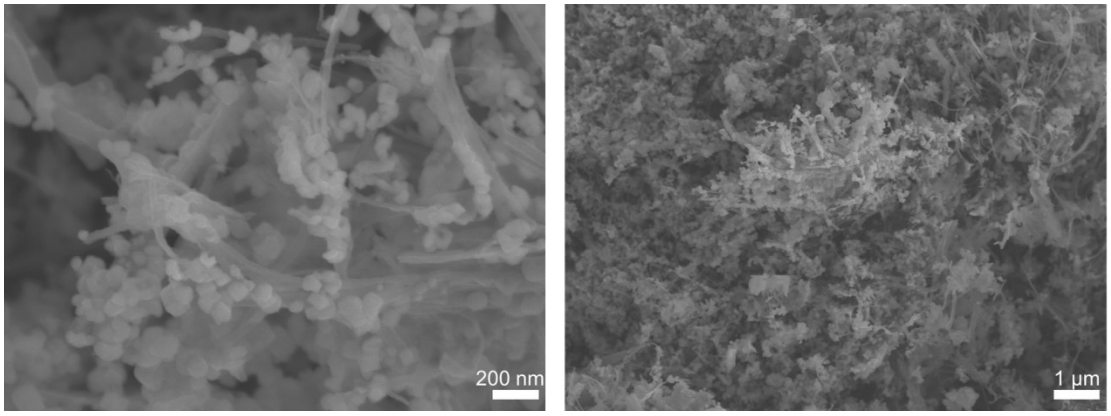

Fig. S2. SEM images of PBC@FeF_2@C before carbonization.

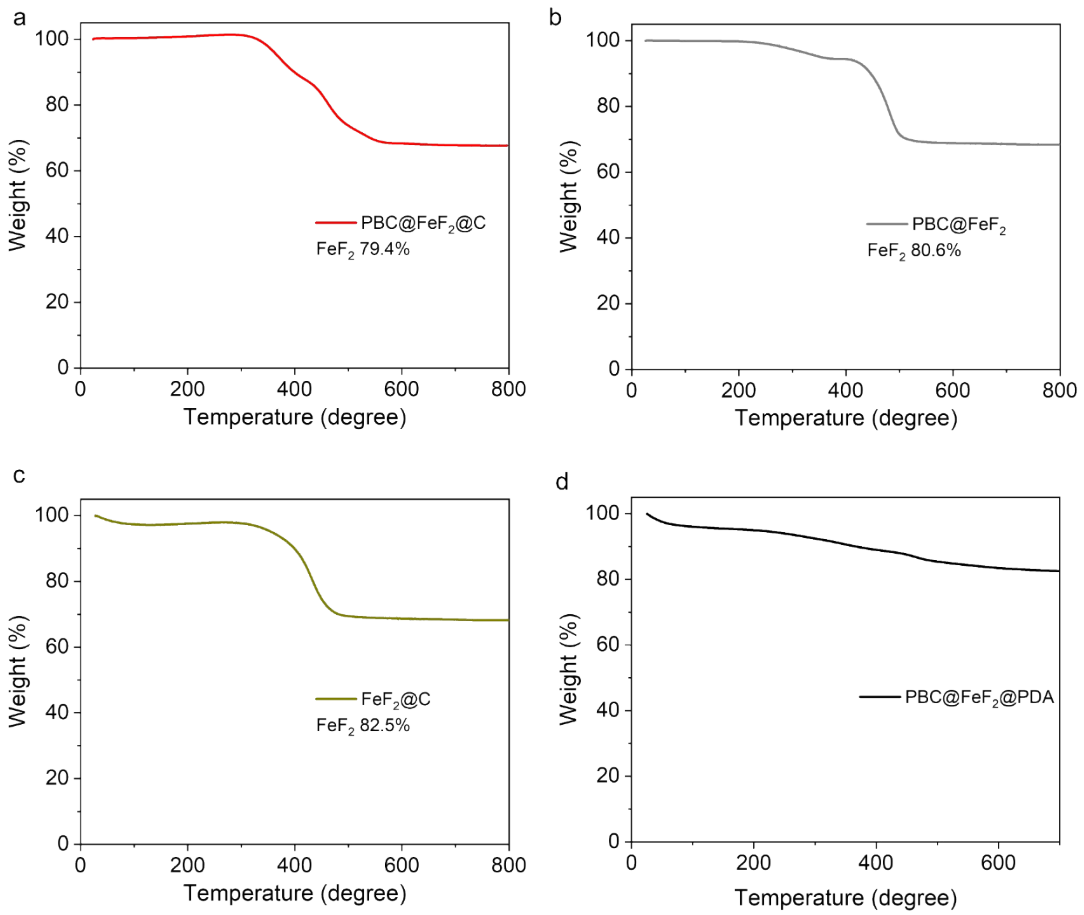

Fig. S3. TGA curves. (a) PBC@FeF_2@C. (b) PBC@FeF_2. (c) FeF_2@C. (d)PBC@FeF_2@PDA.

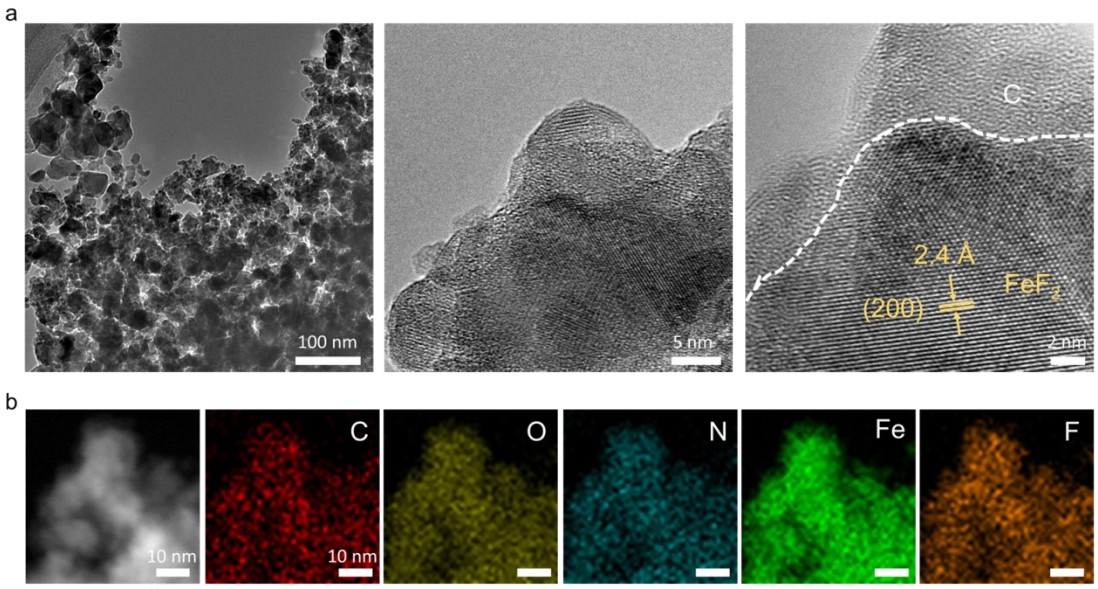

Fig. S4. TEM characterizations of FeF_2@C. (a) TEM images. (b) STEM and elemental mapping images.

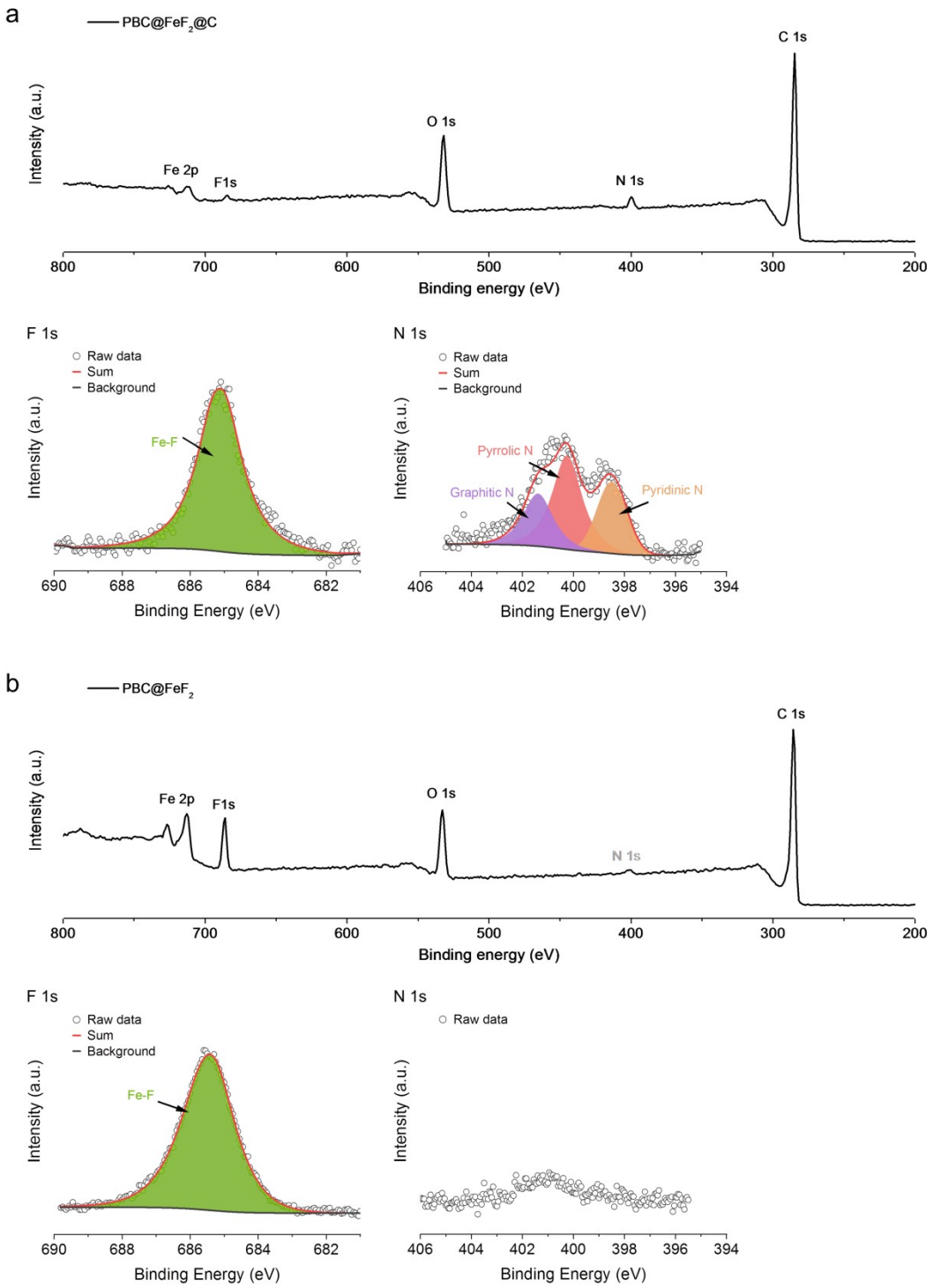

Fig. S5. XPS survey as well as high-resolution F 1s and N 1s spectra. (a) PBC@FeF_2@C. (b) PBC@FeF_2.

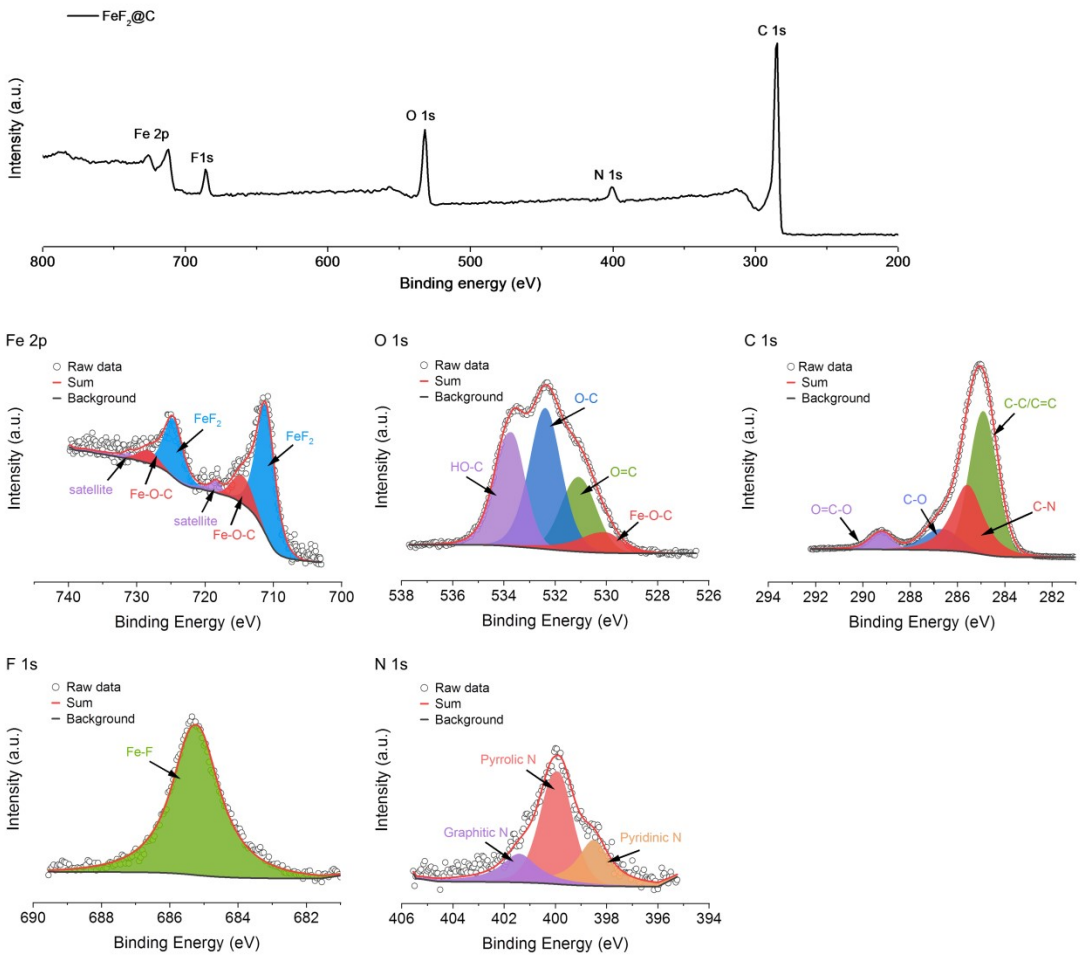

Fig. S6. XPS survey as well as high-resolution Fe 2p, O 1s, C 1s, F 1s, and N 1s spectra of FeF_2@C.

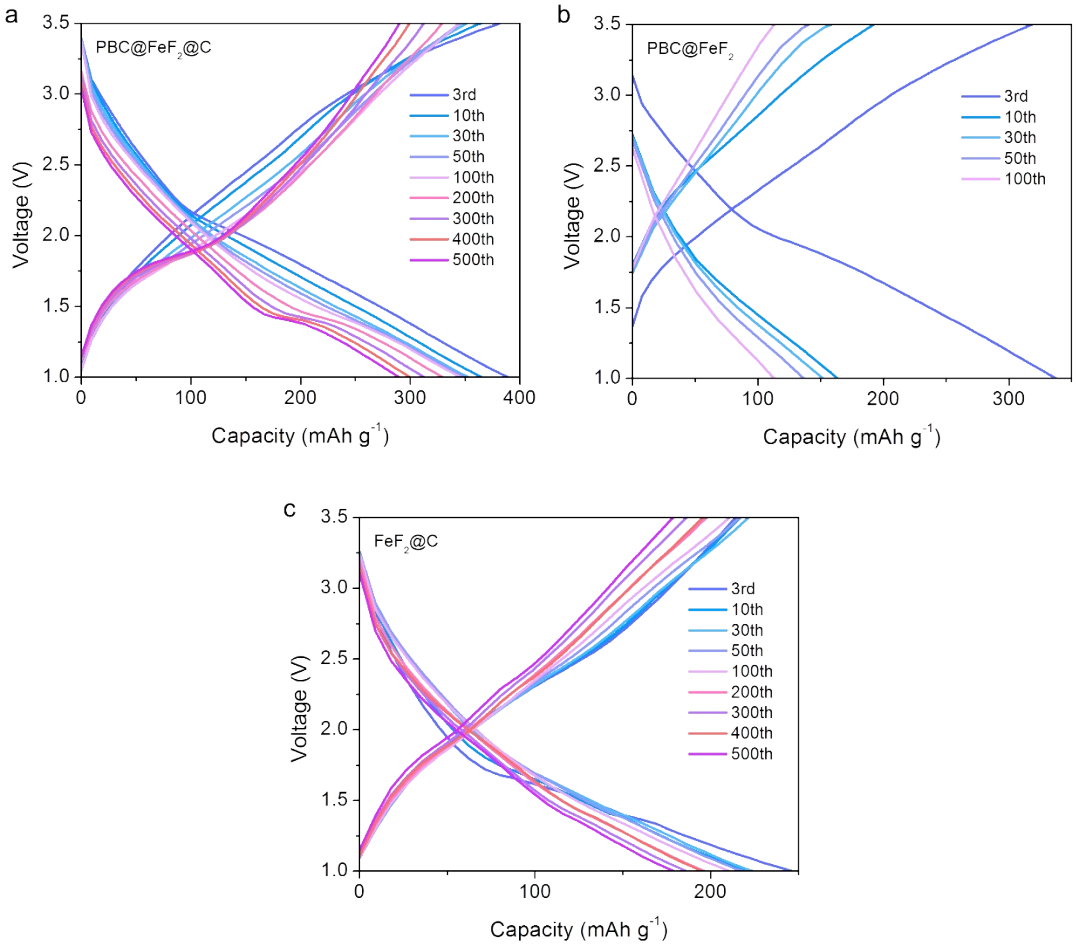

Fig. S7. Galvanostatic charge/discharge profiles at annotated cycles. (a) PBC@FeF_2@C. (b) PBC@FeF_2. (c) FeF_2@C.

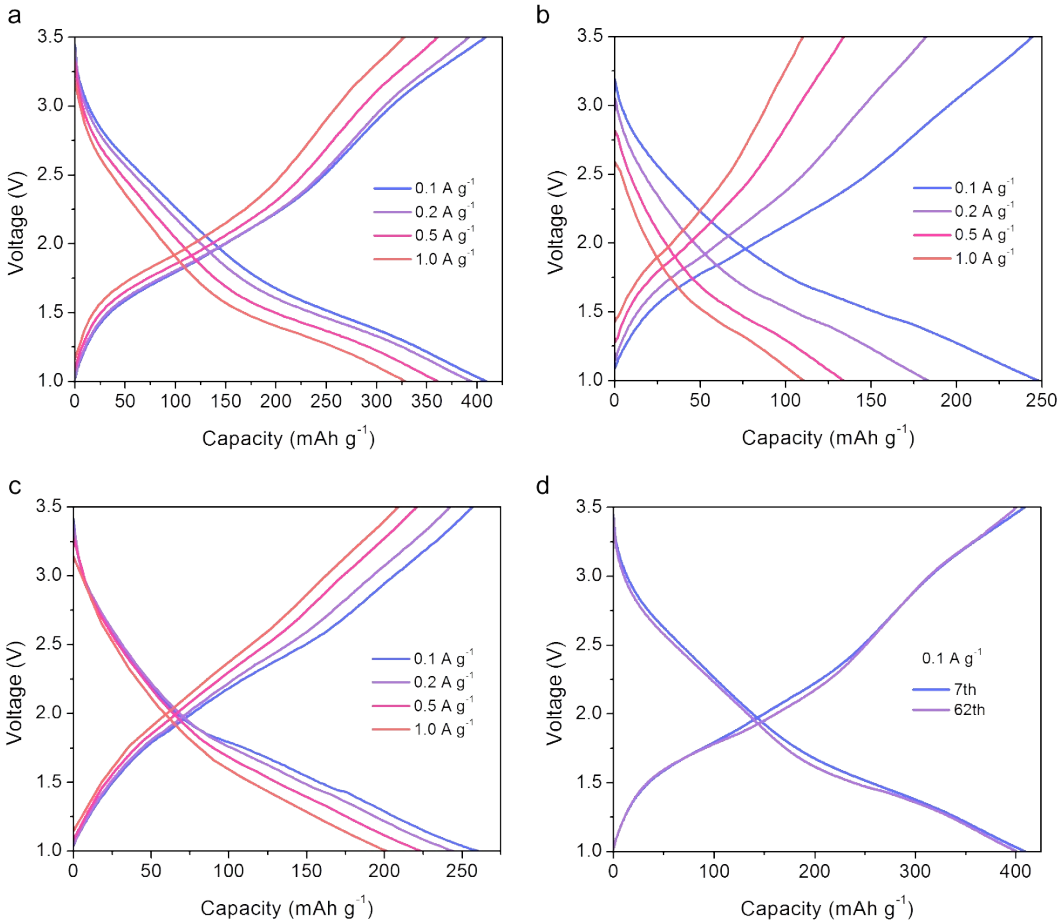

Fig. S8. Galvanostatic charge/discharge profiles at annotated rates. (a) PBC@FeF_2@C. (b) PBC@FeF_2. (c) FeF_2@C. (d) PBC@FeF_2@C before and after rate alternations.

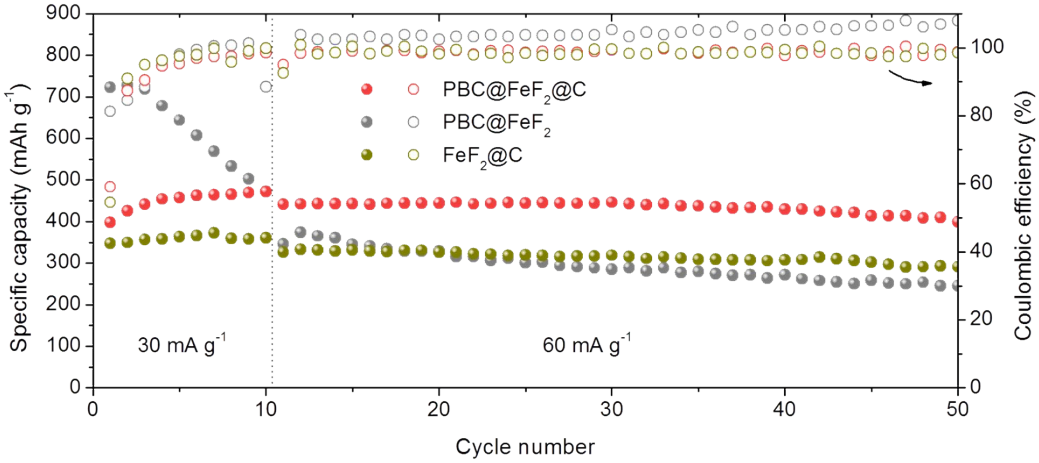

Fig. S9. Cycling performance at annotated rates of PBC@FeF_2@C and control samples in a voltage range of 1.0-3.8 V.

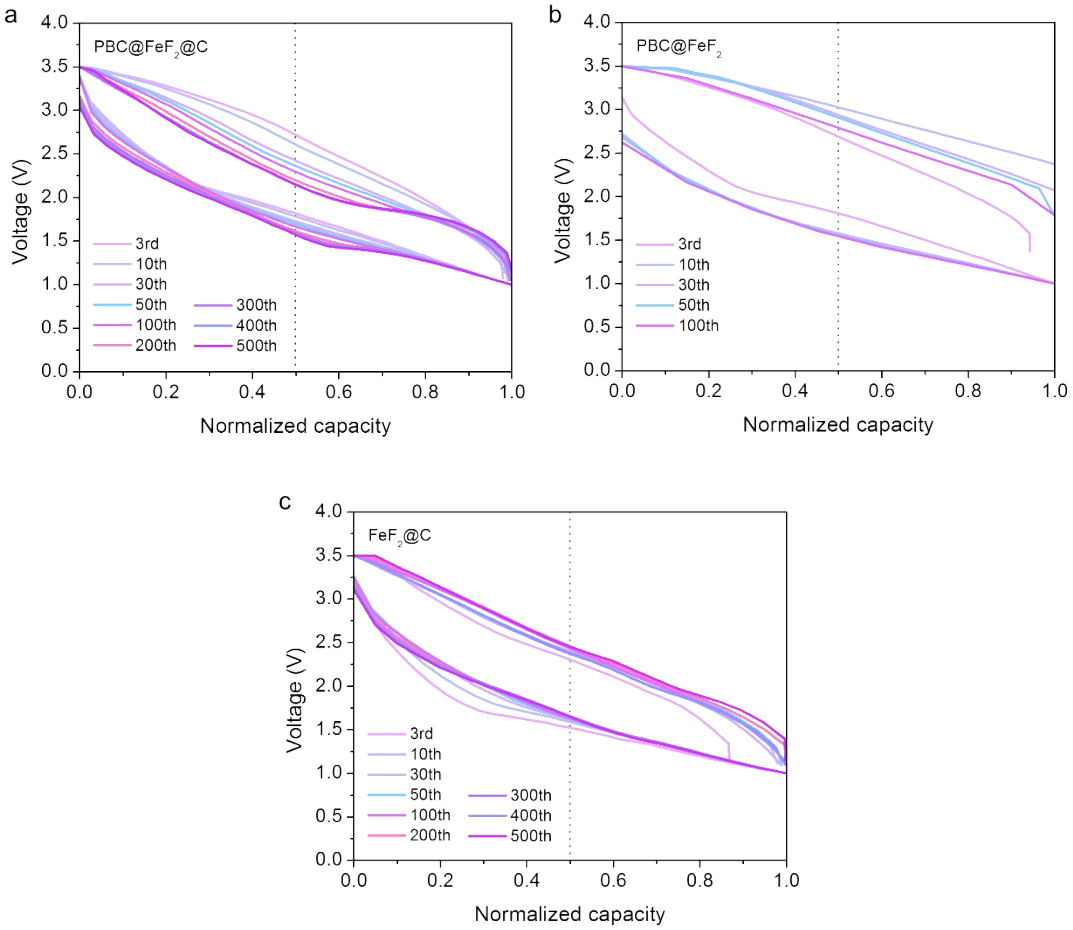

Fig. S10. Galvanostatic charge/discharge profiles with normalized capacity at annotated cycles, demonstrating the variation of overpotential upon cycling. (a) PBC@FeF_2@C. (b) PBC@FeF_2. (c) FeF_2@C.

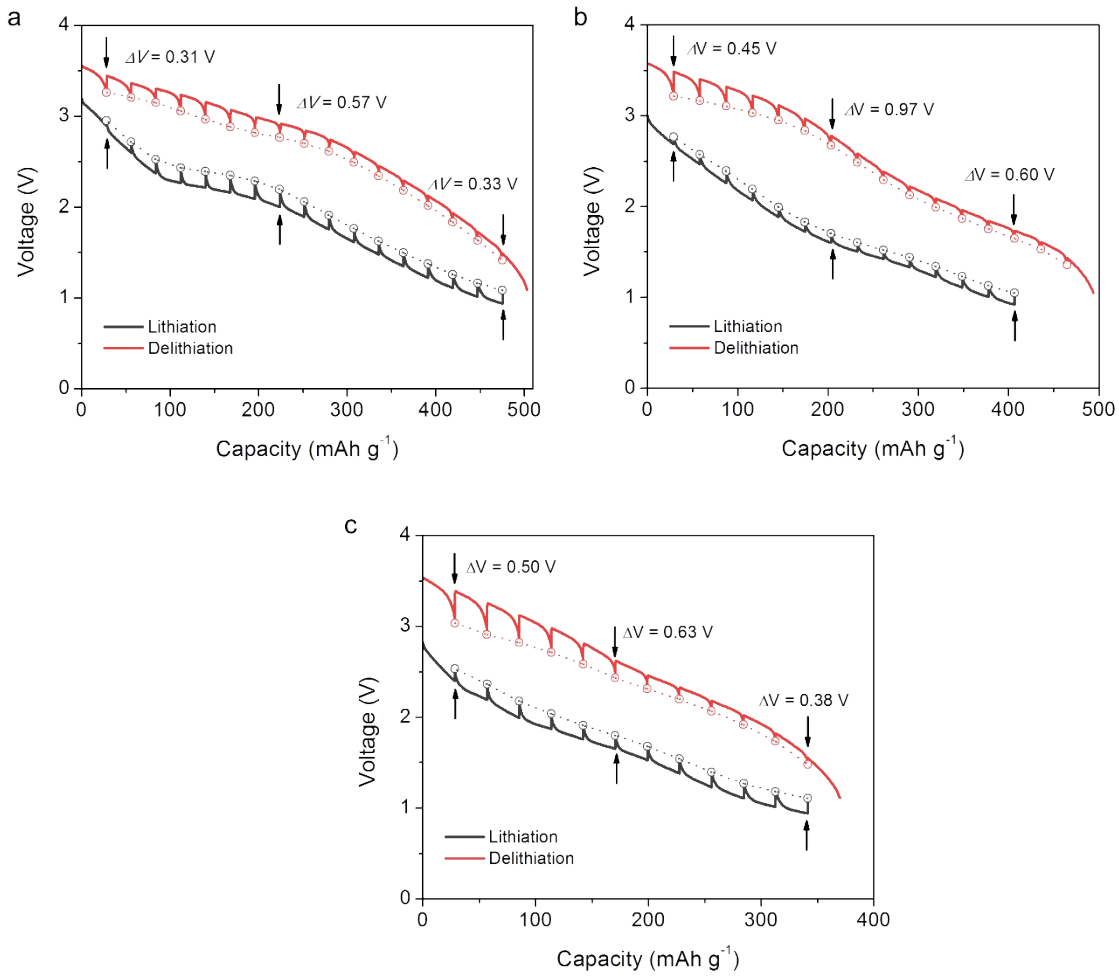

Fig. S11. Galvanostatic intermittent titration technique (GITT) measurements. (a) PBC@FeF_2@C. (b) PBC@FeF_2. (c) FeF_2@C. The hollow circles represent quasi-equilibrium potentials after relaxation at open circuit for 2 h, which is close to thermodynamic values. At the 50 % state of charge/discharge, it is obvious that the quasi-thermodynamic potential hysteresis of PBC@FeF_2@C is only 0.57 V, lower than 0.97 V for PBC@FeF_2 as well as 0.63 V for FeF_2@C.

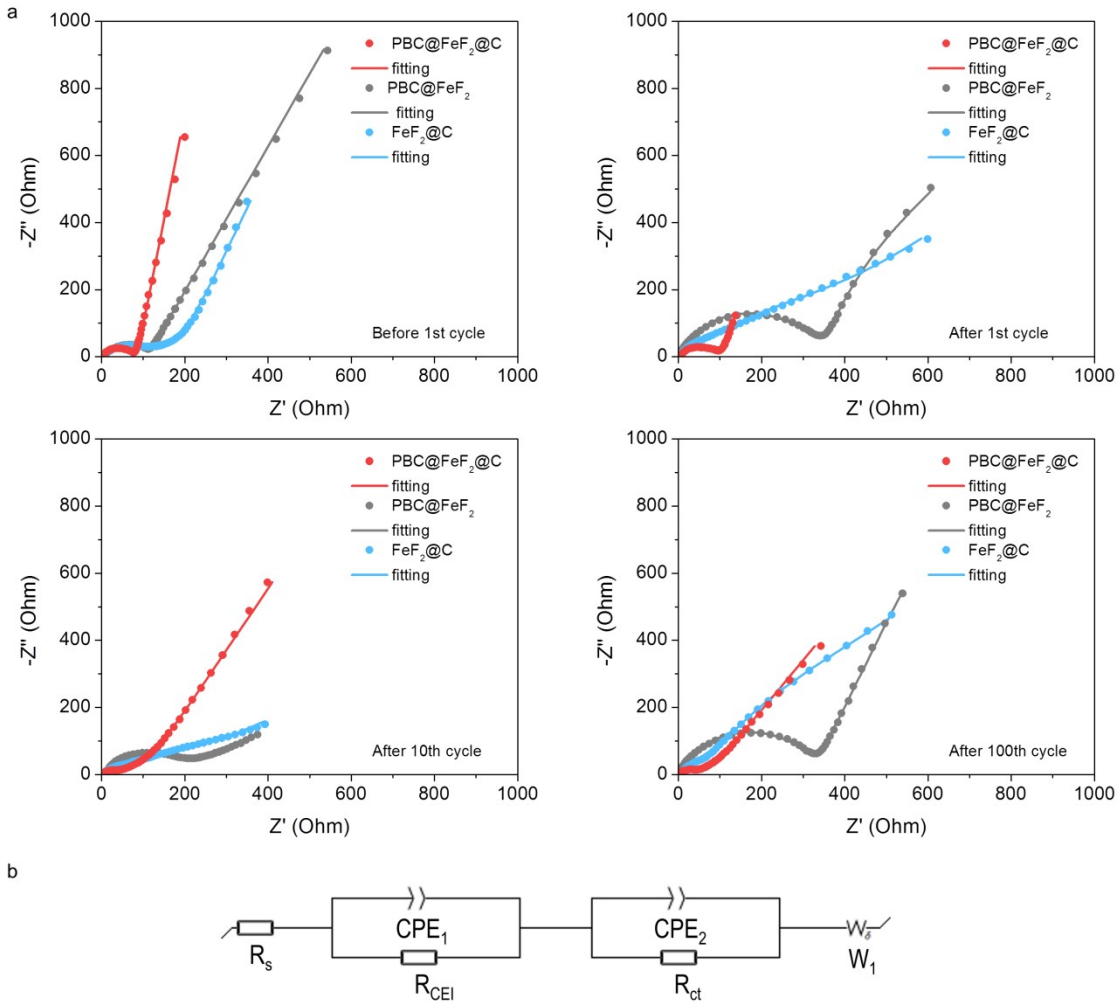

c

	R_s (Ω)			R_{CEI} (Ω)			R_{ct} (Ω)		
	PBC@FeF_2@C	PBC@FeF_2	FeF_2@C	PBC@FeF_2@C	PBC@FeF_2	FeF_2@C	PBC@FeF_2@C	PBC@FeF_2	FeF_2@C
Before 1st cycle	3.8	2.6	1.0	14.2	87.4	87.0	56.6	11.3	98.2
After 1st cycle	2.9	0.6	0.6	20.9	318.5	53.2	71.9	298.3	179.1
After 10th cycle	3.6	8.4	2.1	11.6	166.1	46.6	35.9	486.7	258.7
After 100th cycle	1.2	0.8	5.0	8.2	320.4	28.8	15.1	236.8	215.1

Fig. S12. Nyquist plots, fitting circuit, and resistances of PBC@FeF_2@C and control samples, obtained from EIS measurements. (a) Nyquist plots. (b) Equivalent circuit diagram. (c) Fitted R-values for annotated cycles. Upon cycling, PBC@FeF_2@C invariably exhibits significantly smaller system resistance, CEI resistance, and charge transfer resistance, when being compared to PBC@FeF_2 and Fe@F_2.

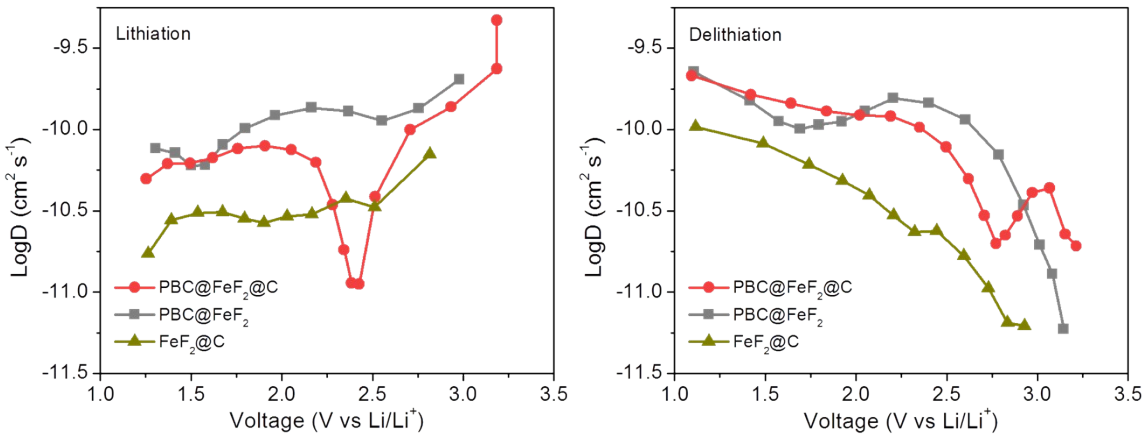

Fig. S13. Lithium diffusion coefficients (D) during discharging (lithiation) and charging (delithiation).

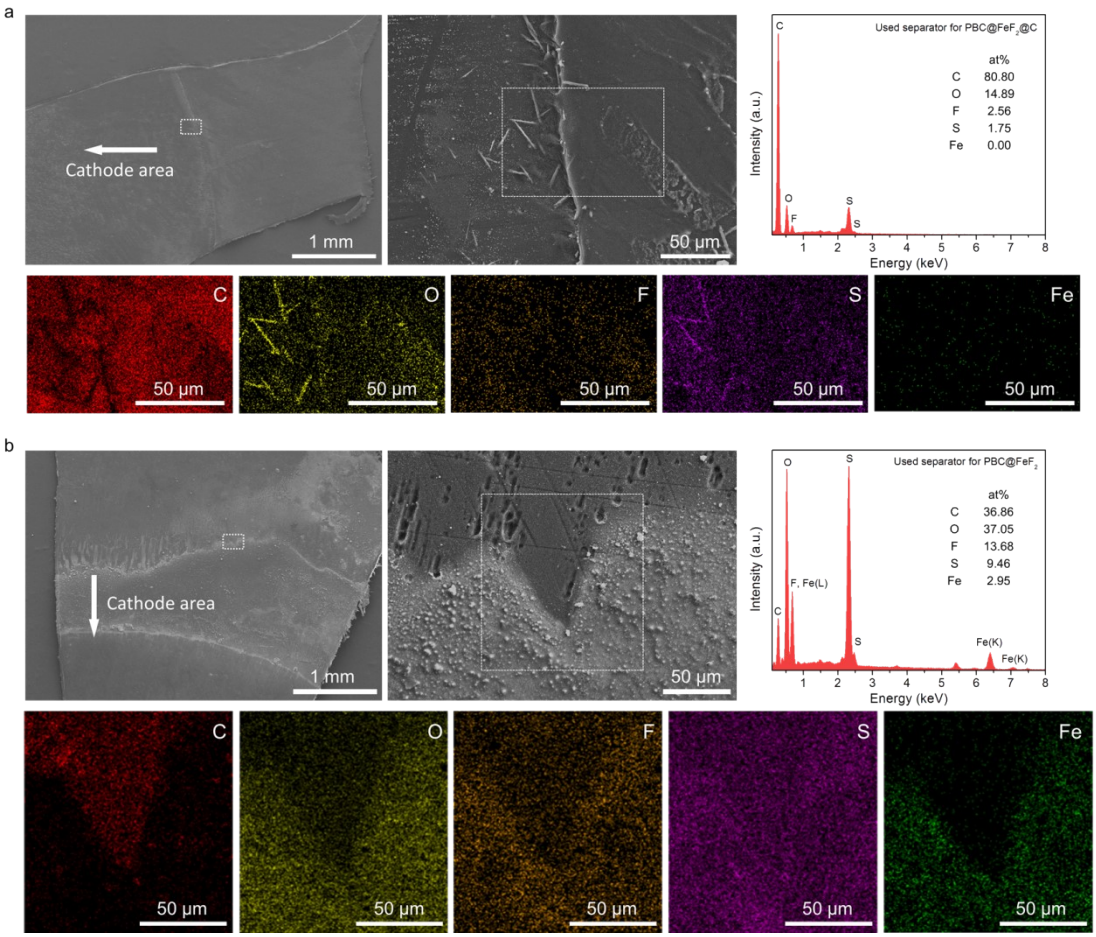

Fig. S14. SEM images, EDX spectrum, and elemental mapping images of cycled separators. (a) Pairing with PBC@FeF_2@C. (b) Pairing with PBC@FeF_2.

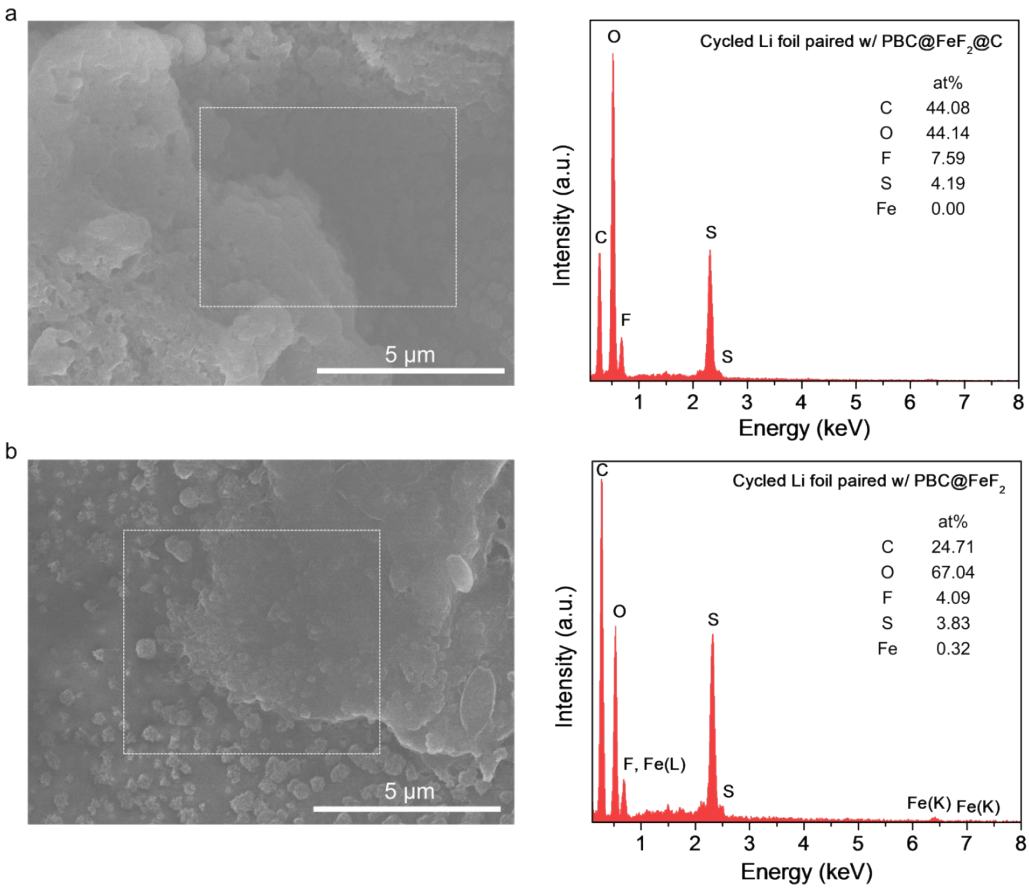

Fig. S15. SEM image and EDX spectrum of cycled Li foils. (a) Pairing with PBC@FeF_2@C. (b) Pairing with PBC@FeF_2.

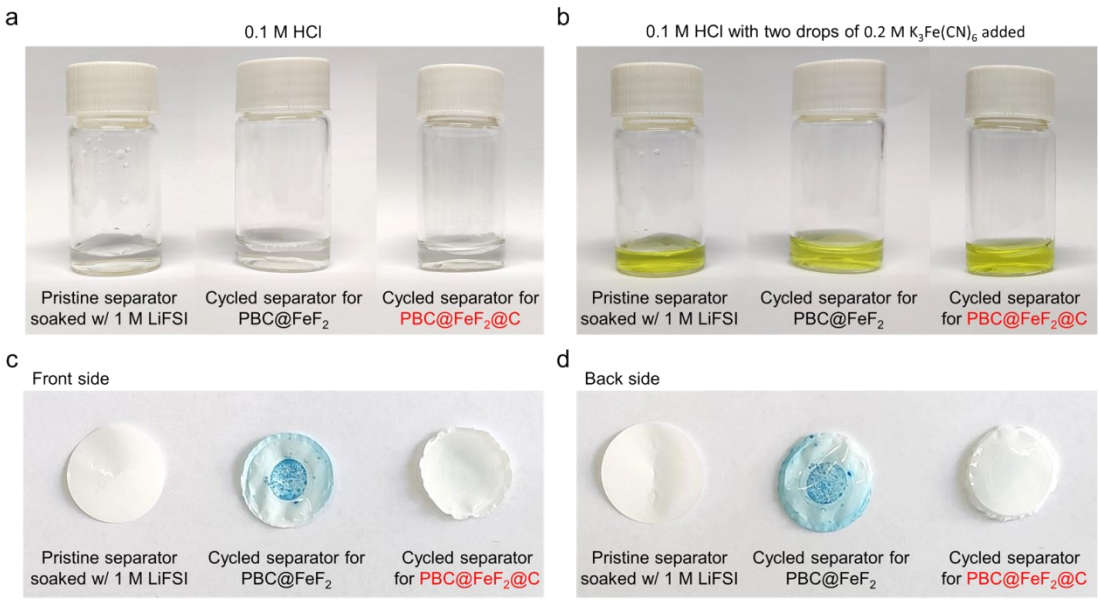

Fig. S16. Determination of Fe species by coloration. (a) Annotated separators immersed in 2 ml of 0.1 M HCl aqueous solution. (b) The solutions with adding 2 drops of 0.2 M $K_3Fe(CN)_6$ aqueous solution and keeping in the dark for 12 h before drying. (c, d) Photo images of treated separators by the above method with (c) Front side and (d) Back side. The intense blue coloration observed in cycled separator for PBC@FeF_2 arises from the reaction of ferricyanide ions ($Fe(CN)_6^{3-}$) with ferrous ions (Fe^{2+}) in acidic solution to produce insoluble blue precipitate ($Fe_3[Fe(CN)_6]_2$), referred to as $3Fe^{2+} + 2[Fe(CN)_6]^{3-} = Fe_3[Fe(CN)_6]_2\downarrow$. By contrast, there is no blue staining in the cycled separator with PBC@FeF_2@C, identifying the absence of any dissolved Fe species.

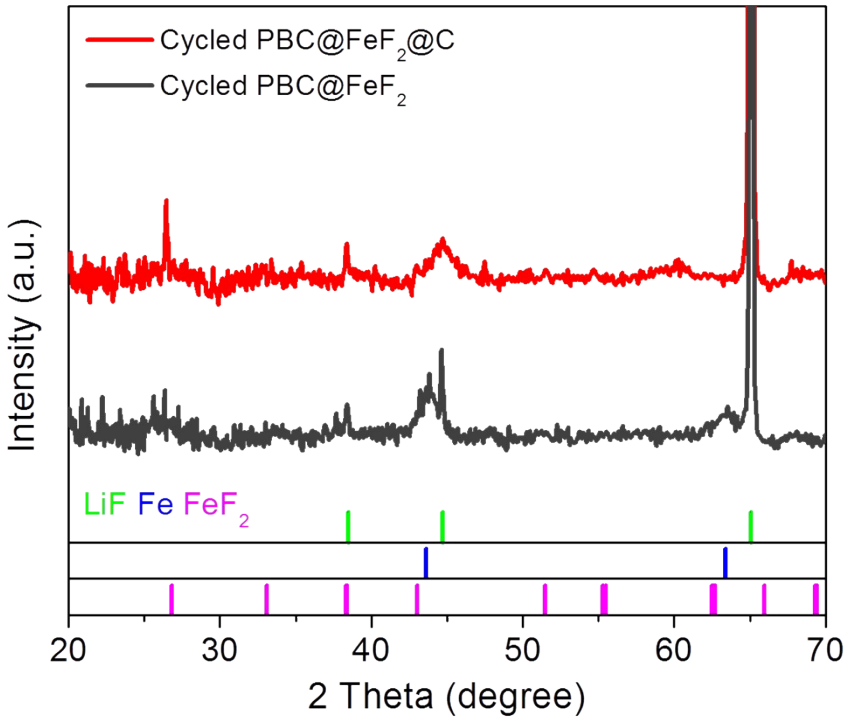

Fig. S17. XRD patterns of cycled PBC@FeF_2@C and PBC@FeF_2. The typical reflections of FeF_2 can be readily recognized in PBC@FeF_2@C, without accompanying metallic Fe, in opposition to the case of cycled PBC@FeF_2. Note that the appearance of lithium fluoride (LiF) in both cases is related to the CEI formed during cycling. Note that the peak at ~65° partially originates from the Al foil used in the cathodes.

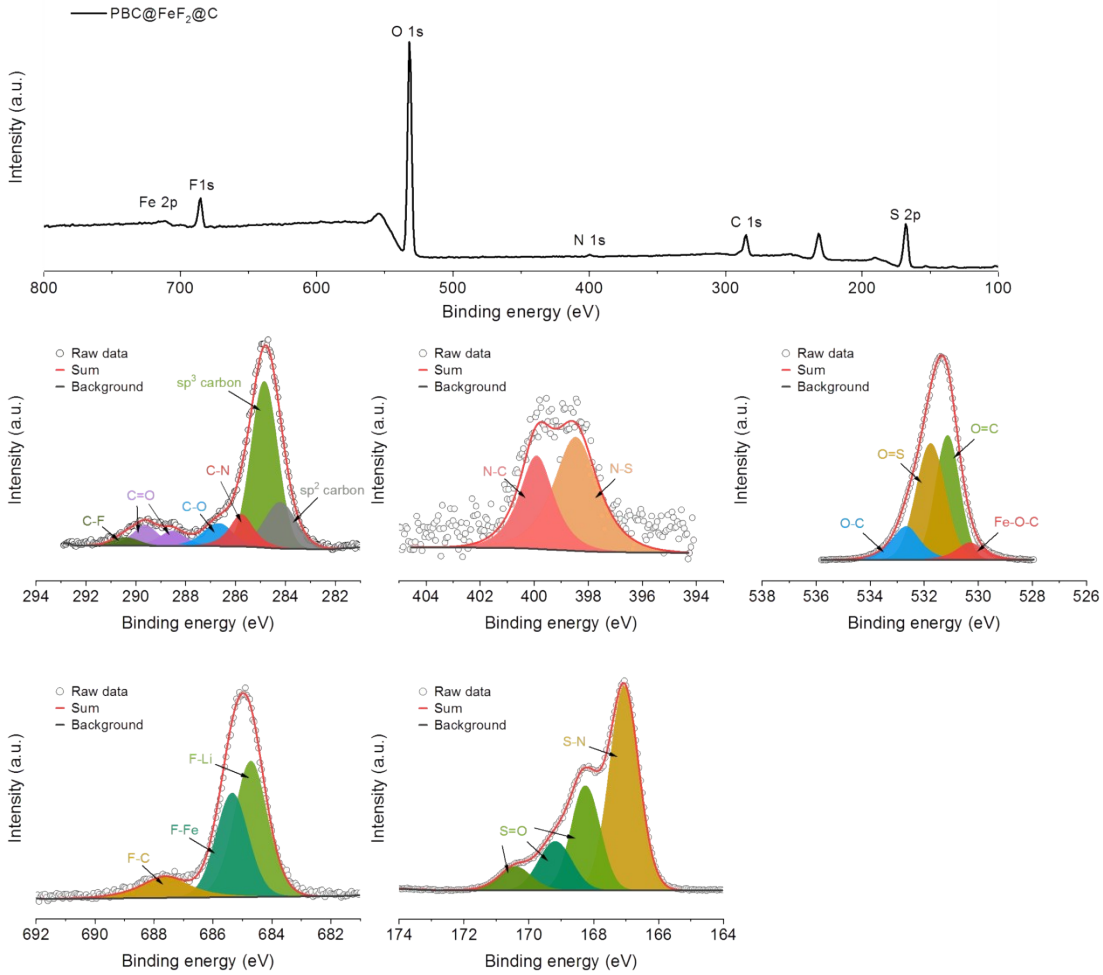

Fig. S18. Survey as well as C 1s, N 1s, O 1s, F 1s and S 2p XPS spectra for cycled PBC@FeF_2@C.

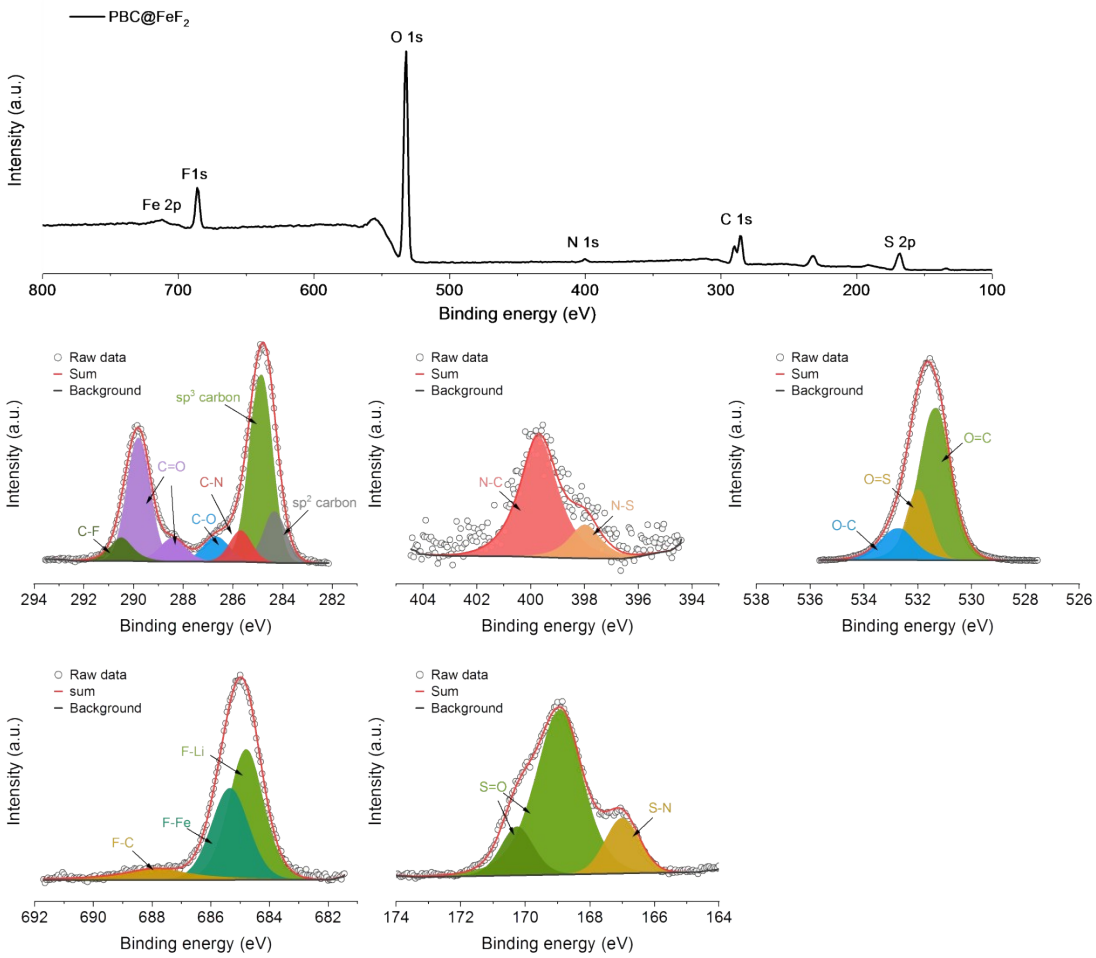

Fig. S19. Survey as well as C 1s, N 1s, O 1s, F 1s and S 2p XPS spectra for cycled PBC@FeF_2.

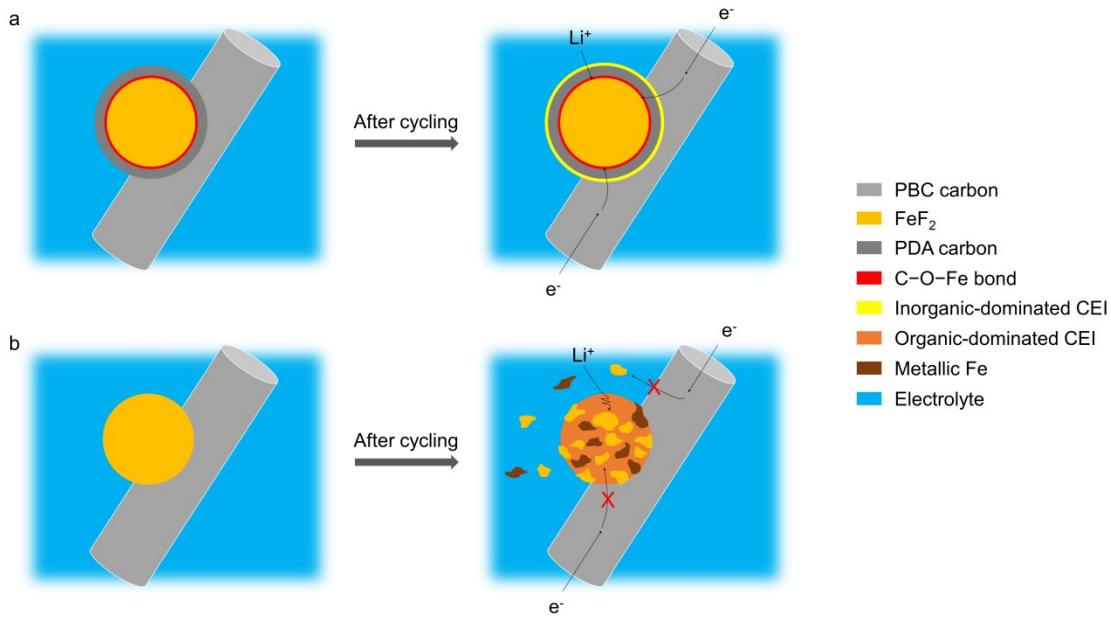

Fig. S20. Schematic description of the stabilization mechanism. (a) PBC@FeF_2@C, (b) PBC@FeF_2. The covalently-bound PDA carbon in PBC@FeF2@C fosters inorganic-dominated CEI, which collaboratively forms a robust and efficient barrier restraining the undesirable material/electrolyte interaction and intractable dissolution. It is noteworthy that the material dimension and interfacial thickness is not scaled.

Table S1. Specification and electrochemical performance. Some representative FeF_2 cathode materials evaluated at similar testing conditions to this work are presented along with PBC@FeF_2@C.

No.	Material	Weight ratio (%) of FeF_2 relative to the material	Material ratio (%) in the electrode	Electrolyte	Voltage window (V)	Current rate (mA g^{-1})	Capacity (mAh g^{-1}) @ achieved *n* cycles	Ref.
1	Porous carbon-confined FeF_2	75	85	**1 M** $LiPF_6$ in DEC/DMC (1:1) with VC	1.5~4	150	120 @ 200	32
2	CF_x derived carbon–FeF_2 composite	/	90	**1 M** $LiPF_6$ in EC/DMC	1.3~4.3	22.7	325 @ 25	36
3	Carbon coated FeF_2	67	70	**1 M** $LiPF_6$ in EC/DMC	1.3~4.2	300	330 @ 100	28
4	FeF_2 film with vertically structured pores	/	/	**1 M** $LiPF_6$ in EC/DMC	1~4.5	12.5	320 @ 10	35
5	Carbon nanotube encapsulated FeF_2 nanorods	71	80	**1 M** $LiPF_6$ in EC/DMC	1~4.2	50	263 @ 50	33
						500	124 @ 50	
						1000	92 @ 50	
6	FeF_2-carbon core-shell composite	62	90	**1 M** $LiPF_6$ in EC/DMC	1.3~4.2	30	350 @ 50	34
7	Ni@FeF_2@Al_2O_3	/	/	**1 M** $LiClO_4$ in EC/DMC	1.2~4.2	200	250 @ 100	31
8	Artificial cathode solid electrolyte interphase-involved FeF_2	100	70	**1 M** LiTFSI in FEC/EMC	1~4	100	314 @ 100	27
9	Dendrite-structured FeF_2	100	70	**1 M** $LiPF_6$ in EC/DEC	1.5~4	200	145 @ 250	29
10	Single-crystalline FeF_2 nanorods	100	70	**1 M** LiFSI in $Pyr_{1,3}FSI$	1.2~4	230~300	300 @ 200	14
11	Porous reduced graphene oxide-FeF_2@carbon	/	70	**1 M** LiTFSI in DOL/DME	1~4	80	400 @ 50	30
12	**PBC@FeF_2@C**	79	80	**1 M** LiFSI in DME	1~3.5	**500**	**290 @ 500**	**In this work**
						2000	**211 @ 102**	